



Switching and control mechanism between p-type and n-type in SnO₂ nanorods using laser with added convex lens to control oxygen concentrations

Changhyun Jin^{a,b,1}, Hyunseong Yang^{a,1}, Kyu Hyoung Lee^{a,*}, Wooyoung Lee^{a,*}

^a Department of Materials Science and Engineering, Yonsei University, Seoul 03722, Republic of Korea

^b KIURI Institute, Yonsei University, Seoul 03722, Republic of Korea

ARTICLE INFO

Keywords:

Gas sensors
Oxidation
Reduction
SnO₂
Semiconductor

ABSTRACT

In a significant advancement, a novel technology has been developed to precisely control the electronic sensitization of SnO₂ nanorods. This control is accomplished in a matter of seconds through the external injection of energy via laser and convex lens pairs (LCP). Utilizing LCP, selective redox reactions can be induced on the surface of SnO₂ nanorods. The study focused on the contrasting effects of NO₂, an oxidizing gas, and H₂, a reducing gas. In the presence of NO₂, the electronic sensitization caused by LCP outweighs the chemical sensitization due to NO₂, thereby resulting in both n-type and p-type behaviors. In contrast, when exposed to H₂, the nanorods exhibit only n-type behavior, as the chemical sensitization effect of H₂ is more significant than the electronic sensitization effect of LCP. The observed variations in electronic properties can be systematically accounted for by the differential bonding energies between oxidizing and reducing gases.

1. Introduction

Metal oxide-based semiconductors are widely employed in applications such as energy conversion and storage [1], optoelectronics [2], light emission [3], high-k gate dielectric [4], photocatalyst [5], photo-detector [6], and gas sensor [7]. These semiconductors are predominantly categorized as either n-type, abundant in electron carriers, or p-type, rich in hole carriers. For the optimal utilization of either electrons or holes in accordance with specific requirements, it is imperative to precisely forecast and regulate the type, quantity, and mobility direction of carriers within the material [8,9]. In the context of intrinsic semiconductors, the thermal energy available at ambient temperature is notably inadequate for the spontaneous generation of mobile carriers, necessitating artificial means for their creation to fulfill diverse functionalities. Given that thermal effects on current semiconductors remain constant, three principal external approaches exist for modulating the carrier concentration and thereby determining the electronic state of the semiconductor.

The first approach involves the deliberate introduction of dopants into the semiconductor material to disrupt existing bonds, thereby augmenting the concentration of surplus electrons or holes [10–12]. The

second strategy pertains to the configuration of electrodes at both ends of the semiconductor; the direction and magnitude of the applied voltage dictate the mobility and quantity of carriers within the semiconductor [13–15]. Finally, the third method capitalizes on photonic energy; when a semiconductor is illuminated with light possessing energy greater than the electrons' binding energy to atoms, electrons overcome these binding energies and become mobile [16–18]. Thus, variations in light intensity or exposure duration can lead to fluctuations in the number of generated electron carriers.

All three methods discussed—introduction of dopants, application of voltage, and exposure to light—utilize external energy sources to perturb the intrinsic semiconductor's thermal equilibrium. This disturbance facilitates the breaking of atomic bonds and subsequent generation of ion-electron pairs: immobile ion carriers and mobile electron (or hole) carriers.

In particular, for semiconductor gas sensors, various photoactivation principles have been used, such as electron/hole pair excitation by visible-light irradiation, the adsorption/desorption control of oxygen and target gas by light induction, and formation of point defects on the surface, such as oxygen vacancies. For example, Zhang et al. [19] demonstrated that when visible light ranging between 400–700 nm was

* Corresponding authors.

E-mail addresses: khlee2018@yonsei.ac.kr (K.H. Lee), wooyoung@yonsei.ac.kr (W. Lee).

¹ Changhyun Jin and Hyunseong Yang had equal contribution as co-first authors.

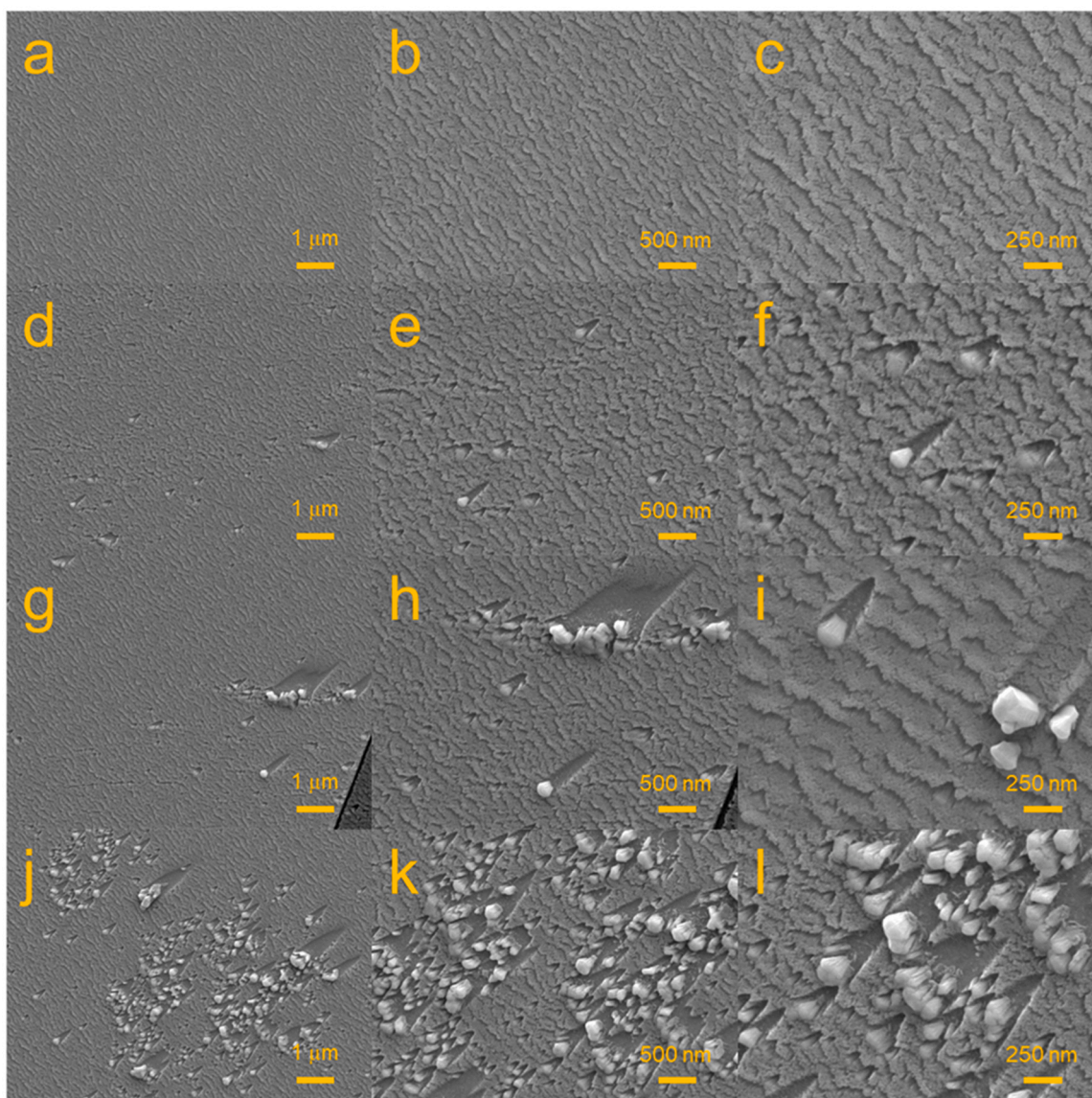


Fig. 1. SEM images illustrating morphological variations in SnO₂ NRs subject to different LCP conditions. Panel (a-c) displays typical SnO₂ NRs under 0 s LCP, while panels (d) - (l) present SnO₂ NRs mixed with SnO₂ NBs under (d-f) 1S5T, (g-i) 3S5T, and (j-l) 4S5T LCP conditions, respectively.

irradiated on an In₂O₃ nanowire with an energy band gap of approximately 2.8 eV (~445 nm), under the condition of $\lambda < 445$ nm, a photogenerated electron-hole pair was created and the adsorbed O_{2(ads)} ions were converted to O_{2(gas)}, presenting a decrease in the resistance of n-type In₂O₃. Additionally, under the condition of $\lambda > 445$ nm, they demonstrated that surface oxygen O_{2(ads)} can be absorbed, desorb O₂ and provide trapped electrons to In₂O₃. Thathsara et al. [20] reported that oxygen gas (O_{2(gas)}) can be converted into photoinduced oxygen ions (O₂⁻) at room temperature via UV illumination of ZnO, which can then participate in the redox reaction of hydrogen sensing. Along with the density functional theory (DFT) calculations of SnO₂ nanowires, Kwon et al. [21] demonstrated that laser-induced oxygen vacancies form excess electrons on the SnO₂ surface, increasing the NO₂ response to over 70.

Crucially, the nature and quantity of mobile carriers in the semiconductor become predetermined once the synthesis process is complete. In essence, the state of electronic sensitization within the semiconductor remains fixed. Given this constant state, adsorption of gases with different bonding energies under uniform temperature conditions results in variable carrier transfers between the semiconductor

and target gases. Therefore, the carrier type, quantity, and movement direction must be sequentially determined based on the nature of the target gas. Despite this complexity, existing literature has largely confined its focus to a rudimentary 2 × 2 matrix—categorizing semiconductors as either n-type or p-type and gases as either oxidizing or reducing. This limited approach has merely emphasized the dichotomous behavior observed in gas sensing applications, where oxidizing and reducing gases manifest opposing behaviors in each category of semiconductor.

In this study, our approach departs from conventional methodologies by introducing a highly-focused energy source via a self-assembled laser beam and convex lens pairs (LCP) to SnO₂ nanorods (NRs) under various conditions. By doing so, both oxidation (Sn: O = 1: 2 +x) and reduction (Sn: O = 1: 2-x) states were precisely modulated relative to the stoichiometric SnO₂ NRs (Sn: O = 1: 2). Notably, a specialized gas-sensing mechanism was revealed: NO₂, an oxidizing gas, induced both n-type and p-type semiconductor behaviors depending on its oxidation level, while all reducing gases exhibited only n-type behavior. The underlying mechanism for this bifurcated response was found to be the preferential electronic versus chemical sensitization reactions with the target gases.

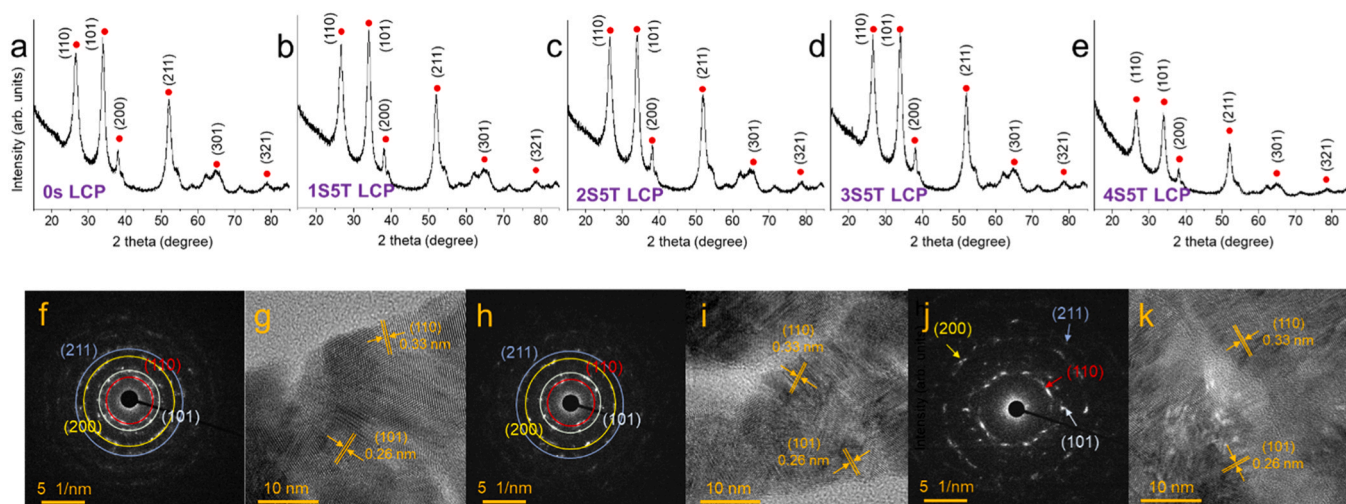


Fig. 2. Characterization of SnO₂ NRs through XRD spectra, SAED patterns, and HRTEM images, segmented by LCP conditions. Panels (a) through (e) show XRD patterns from SnO₂ NRs under various LCP conditions (0 s, 1S5T, 2S5T, 3S5T, 4S5T LCP); panels (f), (h), and (j) exhibit SAED patterns with circumscribed circles signifying polycrystallinity at 0 s, 2S5T, and 4S5T LCP; and panels (g), (i), and (k) illustrate HRTEM interplanar spacing of the (110) and (101) planes at 0 s, 2S5T, and 4S5T LCP, respectively.

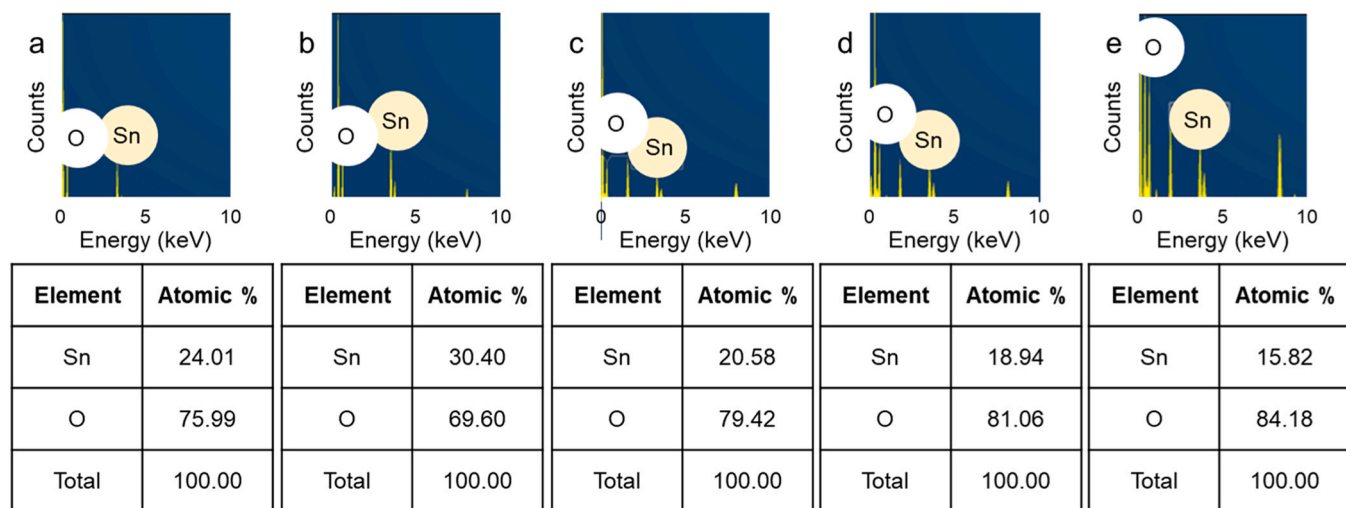


Fig. 3. Elemental composition alterations of Sn and O in SnO₂ NRs across distinct LCP conditions. Panels (a) to (e) correspond to 0 s, 1S5T, 2S5T, 3S5T, and 4S5T LCP conditions, respectively.

For NO₂, an oxidizing gas, electronic sensitization was more prominent, mediated by the degree of oxidation achieved through LCP (electronic sensitization > chemical sensitization). Conversely, for reducing gases, chemical sensitization predominated (electronic sensitization < chemical sensitization). As a result, this detailed analysis is will be instrumental in future studies focusing on the complexities of gas sensing mechanisms.

2. Experimental section

2.1. Materials

SnO₂ NRs were grown on a silicon substrate with a natural oxide film utilizing glancing angle deposition (GLAD) with E-beam equipment under a high vacuum condition of 2.0×10^{-6} torr or lower. To ensure uniform deposition, specific parameters were employed: an 80° sample tilt, 12 rpm rotation, and a 30-minute deposition time. Subsequently, the SnO₂ NRs were stabilized via heat treatment at 500 °C. A custom-designed LCP approach at room temperature was adopted for the

surface modification of these SnO₂ NRs. The experimental setup placed a convex lens (23 mm in diameter) 30 cm away from a 650 nm, 200 mW laser, while situating the SnO₂ NRs sample 6.5 cm from the convex lens. To achieve a uniform point defect across the entire sample, the laser point energy was applied in five sequential injections, ranging from 1 s (1S5T) to 4 s (4S5T) (five times for each time point). Specifically, the LCP was applied by moving 1 mm diagonally from the center to the upper left, upper right, lower left, and lower right sides.

2.2. Characterizations

Various advanced characterization techniques were employed to elucidate the morphological, compositional, and crystallographic attributes of the SnO₂ NRs under differing conditions. Field emission scanning electron microscopy (FE-SEM, JSM-7800 F, JEOL Ltd.) and field-emission transmission electron microscopy (FE-TEM, JEM-F200, JEOL Ltd.) were utilized to investigate the sample morphology. Energy dispersive X-ray spectroscopy (EDX) and mapping, integrated into the TEM, further contributed to compositional analysis. For crystallographic

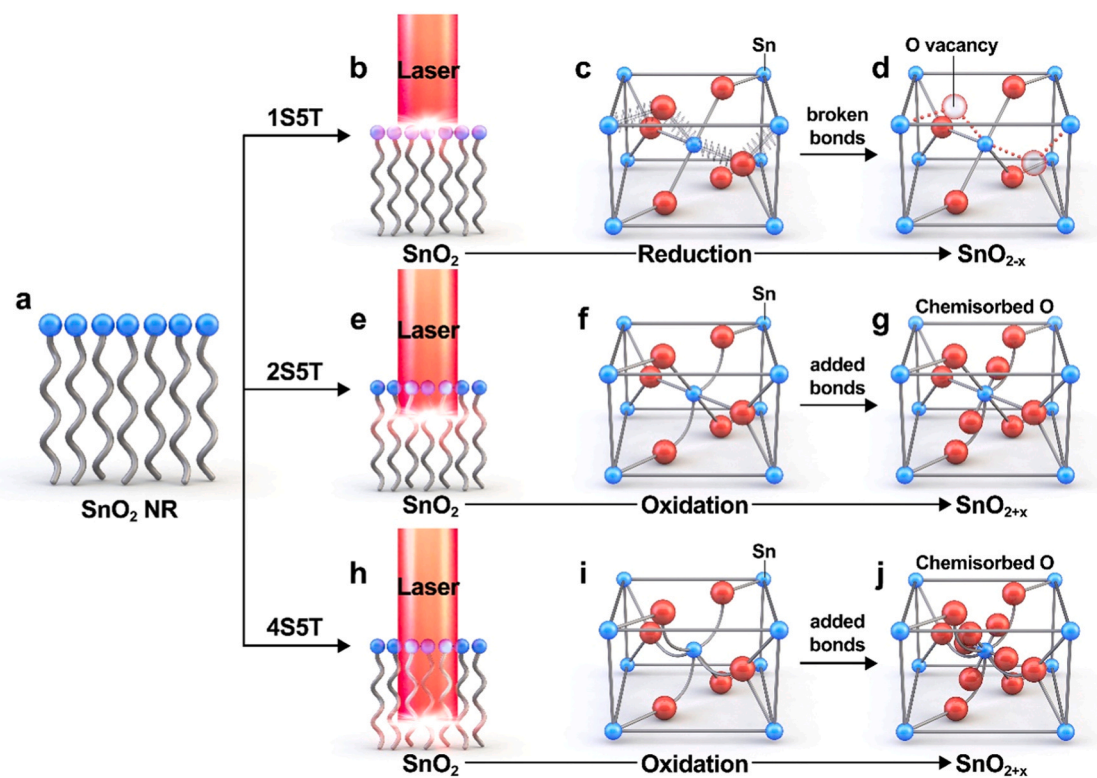


Fig. 4. Schematic representations delineating the chemical transformations in SnO₂ NRs under varying LCP conditions. Panels (a) and (b) showcase SnO₂ NRs at 0 s and 1S5T LCP; panel (c) reveals the disruption of SnO_{2-x} NR bonds under 1S5T LCP; panel (d) depicts the genesis of oxygen vacancies by 1S5T LCP; panels (e) to (j) detail the progressive evolution of SnO₂ NRs, emphasizing bond augmentation and chemisorbed oxygen formations at 2S5T and 4S5T LCP conditions.

Table 1

Types and exhibiting both n-type and p-type characteristics.

Materials	Original semiconductor type	Transitioned semiconductor type	Process method	Process temperature	Application	Ref.
SnO ₂ NRs	n-type	p-type	LCP	RT	Gas sensors	Our work
ZnO nanostructures	n-type	p-type	Cu doping	RT	Gas sensors	[29]
ZnO thin films	n-type	p-type	Ion implantation	700 °C - 950 °C	Thin films	[30]
CuO thin films	p-type	n-type	Magnetron sputtering	> 500 °C	Thin films	[31]
Ga ₂ O ₃ nanostructures	n-type	p-type	H ₂ diffusion	700 °C - 950 °C	high-power devices	[32]
In ₂ O ₃ nanostructures	n-type	p-type	Bi doping	1000 °C - 1200 °C	Transparent conducting oxides	[33]
Bi ₂ O ₃ nanostructures	n-type	p-type	N and H doping	-	photocatalysts	[34]
CuO thin films	p-type	n-type	spin coating	RT	Thin films	[35]
NiO thin films	p-type	n-type	RF magnetron sputtering	RT	Photovoltaic devices	[36]
NiO thin films	p-type	n-type	ultraviolet-laser irradiation	200 °C	Organic light emitting diodes	[37]
TiO ₂ nanostructures	n-type	p-type	Li diffusion	140 °C - 550 °C	Li-ion batteries	[38]

evaluation, X-ray diffraction (XRD; Smart Lab, Rigaku) with Cu-K_α irradiation ($\lambda = 1.5418 \text{ \AA}$), selected area electron diffraction (SAED), and high-resolution transmission electron microscopy (HRTEM) were implemented. X-ray photoelectron spectroscopy (XPS, Thermo Fisher Scientific Co.) and ultraviolet photoelectron spectroscopy (UPS, Thermo Fisher Scientific Co.) were performed to probe the surface properties and energy states of SnO₂ NRs.

2.3. Gas sensing tests

For the gas-sensing experiments, 50 ppm of NO₂ gas (oxidizing) and 50 ppm of H₂ gas (reducing) were used. In addition to the aforementioned process, new SnO₂ NRs were grown on a self-patterned Si/SiO₂

wafer substrate with an oxidation layer of 3000 Å. Immediately before gas sensing, the same LCP process at room temperature was performed once again on the SnO₂ NRs from 1S5T to 4S5T. Gas sensing of the SnO₂ NRs with and without the LCP process was performed in a tube furnace, and the reactive and carrier gases, whose concentrations were adjusted using mass flow controllers (MFCs), were directed into the tube furnace. The concentrations of the target gases were controlled by adjusting the mixtures with dry air. The process temperature of 300 °C and the gas flow rate of 50 ppm were automatically fixed by custom LabView software, and changes in the dynamic electrical resistance under different LCP process conditions (from 0 s LCP (bare SnO₂ NRs) to 4S5T LCP) were measured by a nanovoltmeter (Keithley 2182) using a constant current source of 100 nA (Keithley 6220). Depending on the

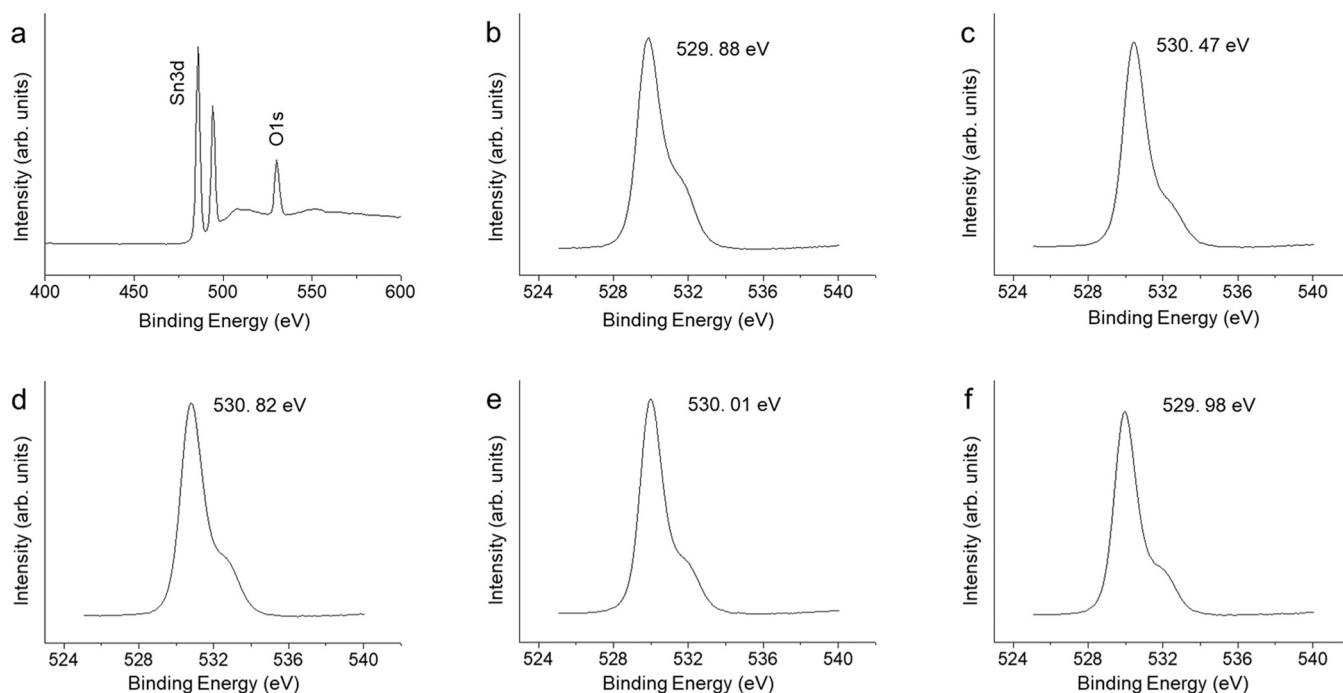


Fig. 5. Variations in binding energy and chemical states of Sn and O subject to specific LCP conditions. Panels (a) and (b) display XPS spectra for SnO₂ NRs under 0 s LCP, whereas panels (c) – (f) illustrates changes in the oxygen peak at 1S5T, 2S5T, 3S5T, and 4S5T LCP conditions, respectively.

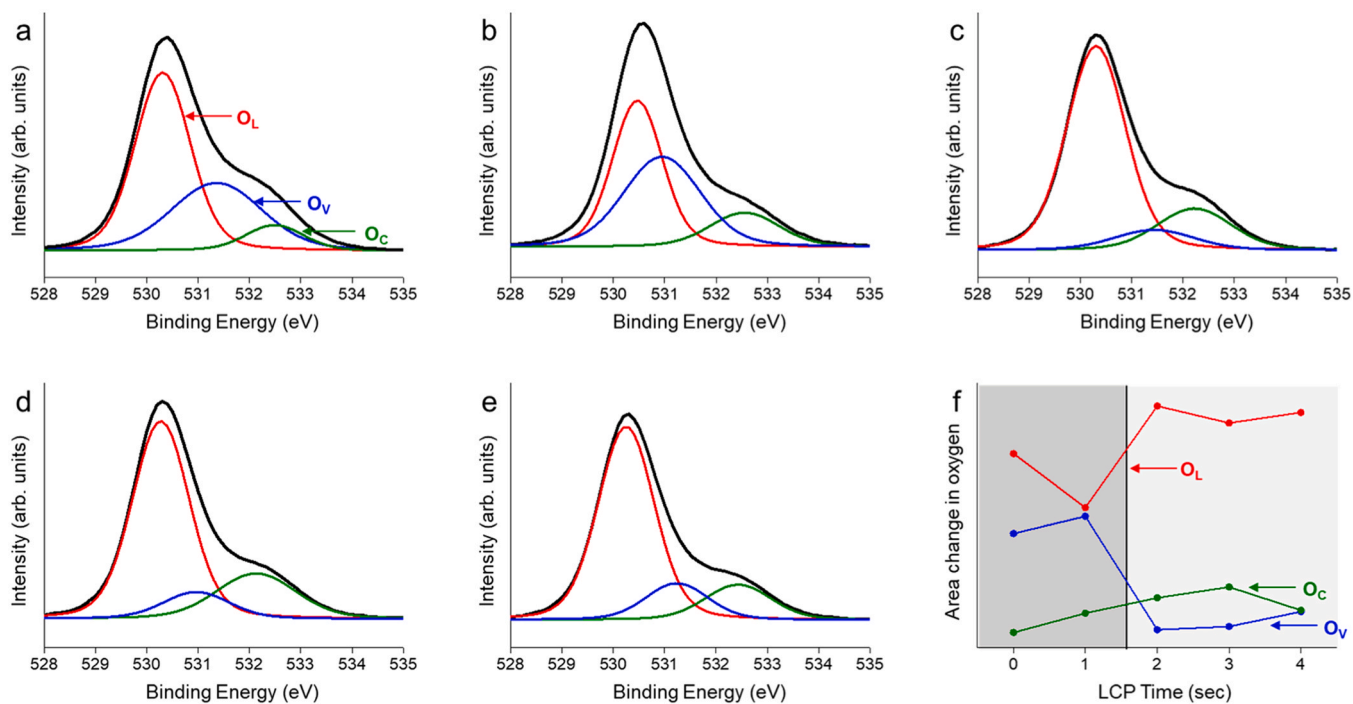


Fig. 6. O 1 s XPS spectrum and decomposed components of SnO₂ NRs with LCP process. Panels (a)-(e) display XPS spectra for SnO₂ NRs at 0 s LCP, 1S5T, 2S5T, 3S5T, and 4S5T LCP conditions, whereas panel (f) illustrates the changes in the type of oxygen contributing, respectively.

stoichiometric state of the SnO₂ NRs, the relationship between air (R_a) and target gases (R_g) explains the gas-sensing response as follows: (1) For NO₂, an oxidizing gas, and n-type semiconductor SnO₂ (Sn: O = 1:2-x), the relationship is R_g/R_a ; (2) for NO₂ and p-type semiconductor SnO₂ (Sn: O = 1:2+x), the relationship is R_a/R_g ; (3) for H₂, a reducing gas, and the n-type semiconductor SnO₂ (Sn: O = 1:2-x), the relationship is R_a/R_g ; and (4) for H₂ and the p-type semiconductor SnO₂ (Sn: O =

1:2+x), the relationship is R_g/R_a . The response and recovery times were defined as the times taken to reach a point corresponding to 90% of the resistance before saturation when the target gas (response time) and air (recovery time) were injected, respectively.

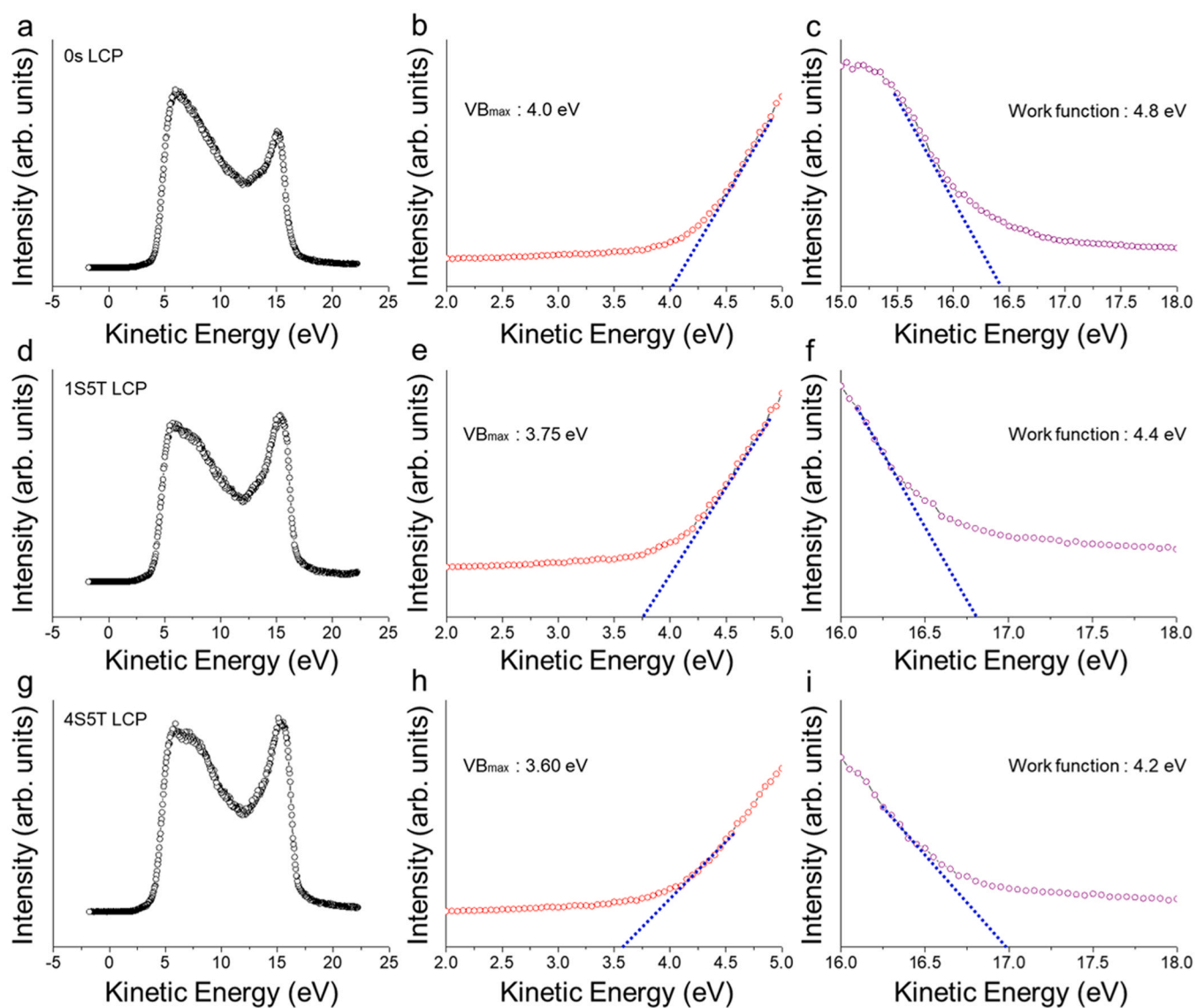


Fig. 7. Variations in work function and valence band maximum in SnO₂ NRs under different LCP conditions: (a) UPS analysis for SnO₂ NRs with 0 s LCP, (b) determination of the valence band maximum at 4.0 eV, and (c) work function evaluation at 4.8 eV with a cutoff energy of 16.4 eV, calculated as the difference between incident energy (21.2 eV) and cutoff energy (16.4 eV). (d) UPS analysis for SnO_x NBs and NRs treated with 1S5T LCP, (e) identification of valence band maximum at 3.75 eV, and (f) work function evaluation at 4.4 eV with a cutoff energy of 16.8 eV, calculated as the difference between incident energy (21.2 eV) and cutoff energy (16.8 eV). (g) UPS analysis for SnO_x NBs and NRs treated with 4S5T LCP, (h) identification of valence band maximum at 3.6 eV, and (i) work function evaluation at 4.2 eV with a cutoff energy of 17.0 eV, calculated as the difference between incident energy (21.2 eV) and cutoff energy (17.0 eV).

3. Results and discussions

Significant alterations in both physical (from NR to nanobead (NB)) [22] and chemical (oxygen vacancy or chemisorbed oxygen) states were observed on the SnO₂ NR surface subsequent to LCP treatment. As illustrated in Fig. 1a-c, the SnO₂ NRs first grew uniformly, as demonstrated by the top view (Fig. 1a). However, at the microscopic level, height differences were observed (Fig. 1b-c). Upon LCP treatment under the 1S5T conditions (Fig. 1d-f), NBs with radii of approximately 100 nm sporadically formed. These NBs resulted from the aggregation of multiple SnO₂ NRs, effectively reducing the total cross-sectional area, and thus the energy of the system. Extending the LCP application to 3S5T (Fig. 1g-i) and 4S5T (Fig. 1j-l) increased the size of these NBs to approximately 100–300 nm and 500 nm–1 μm, respectively. Notably, these results demonstrate that both the physical and chemical properties can be modulated in a time-dependent manner by delivering concentrated energy via LCP.

The crystal structure of SnO₂ NRs as a function of varying LCP conditions was characterized using XRD. As depicted in Fig. 2a-e, under all conditions, the diffraction patterns exhibited peaks corresponding to the (110), (101), (200), (211), (301), and (321) planes, thereby confirming the tetragonal structure of SnO₂ (JCPDF Card No. 01-077-0449) [23]. The XRD also demonstrated that there were no significant changes in the process up to 3S5T LCP according to the intensity (Fig. 2a-d); however, when the LCP process excessively progressed (4S5T LCP) (Fig. 2e), the (110), (101), and (211) planes decreased. Therefore, according to the Scherrer formula ($D = k\lambda/\beta\cos\theta$), where D is the average crystallite size of the particle, k is Scherrer constant (i.e., 0.94), λ is the wavelength of the X-ray (i.e., 0.154), β is the full width at half maximum (FWHM) of the diffraction peak, and θ is the angle of diffraction [24], the 4S5T LCP (Fig. 2e) demonstrated a smaller FWHM at the same location, resulting in a larger crystallite size of the particle (i.e., from 6.66 nm to 6.99 nm), and this was closely related to the formation of SnO₂ NBs according to the LCP. The polycrystalline nature of the structure was further verified

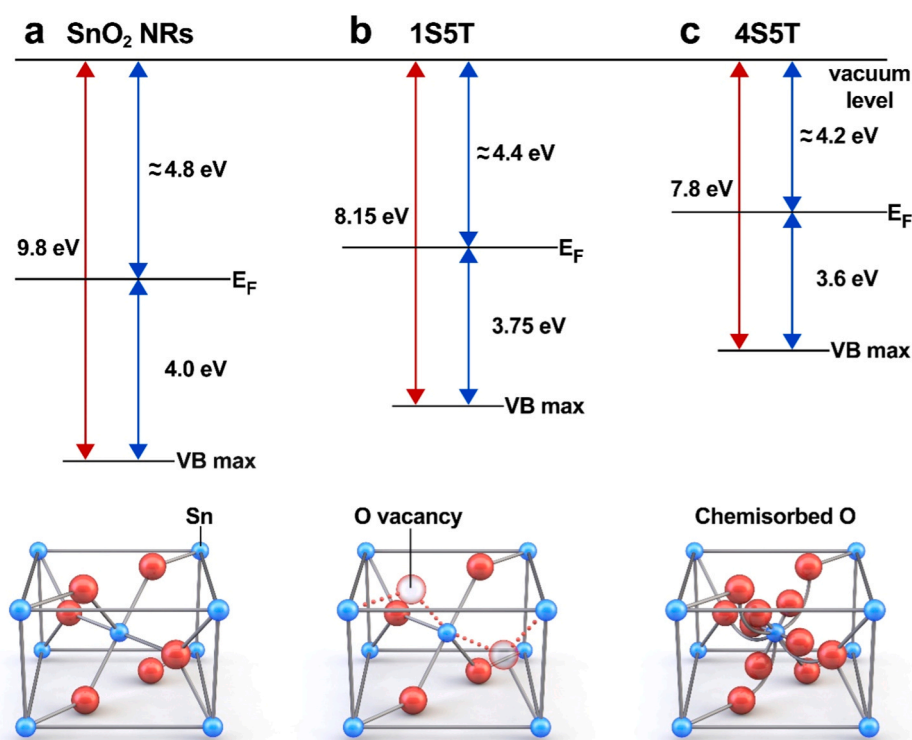


Fig. 8. Schematic band diagram of SnO₂ NRs with LCP process. Panels (a)-(c) indicate the change in energy band of SnO₂ NRs at (a) 0 s LCP, (b) 1S5T, and (c) 4S5T LCP conditions, respectively.

through SAED (Fig. 2f, h, j), while HRTEM (Fig. 2g, i, k) confirmed interplanar spacings of 0.33 nm for the (110) plane and 0.26 nm for the (101) plane.

In regard to compositional alterations, the initial stoichiometry of Sn and O in SnO₂ NRs exhibited dependency on LCP treatment. For instance, NRs subjected to zero-second LCP exposure (0 s LCP) manifested a non-stoichiometric profile marked by high levels of oxygen vacancies, primarily owing to insufficient processing time during synthesis (Figs. 3a and 4a). At an LCP setting of 1S5T, the high-energy LCP disrupted Sn-O bonds, creating an abundance of O vacancies and instigating a reduction reaction from SnO₂ to SnO_{2-x} [25,26] (Fig. 3b and Fig. 4b-d). Conversely, an extension of LCP duration to 2S5T and 3S5T (Fig. 3c-d and Fig. 4e) facilitated deeper penetration of laser energy. Initially, this disrupted Sn-O bonds but subsequently led to localized heat generation, attracting ambient oxygen and inducing the formation of chemisorbed O. This catalyzed an oxidation reaction, transforming SnO₂ to SnO_{2+x} [27,28] (Fig. 3c-d and Fig. 4e-g). Consequently, with extended LCP durations, as in 4S5T (Fig. 3e and Fig. 4h-j), the laser's influence penetrated deeper, yielding a greater number of chemisorbed O on the SnO₂ surface compared to the 2S5T and 3S5T condition.

Even though a material may be composed of the same elements, many semiconducting metal oxides can exist in either p-type or n-type configurations depending on the processing conditions, as illustrated in Table 1 [29–38]. Conventionally, these materials undergo a unilateral transition in electrical type through methods like doping or thermal treatment. However, as observed in our study, this is not an irrevocable change; rather, the electrical type can be modulated bidirectionally through the application of LCP treatment or variations in oxygen concentration. Consequently, LCP emerges as a potent new technique for dynamically modulating the electrical type of semiconductors within a condensed timeframe.

This capability is further substantiated by XPS analyses (Fig. 5). Meanwhile, the theoretical and experimental details regarding point defects in SnO₂ are well-known. For example, Xiong et al. [39]

demonstrated that the types of defects that can occur in SnO₂ are not only typical oxygen vacancies, single-ionized oxygen vacancies, double-ionized oxygen vacancies, tin interstitials, tin vacancies, but also tin antisites, oxygen antisites, bridging oxygen vacancies, subbridging oxygen vacancies, and Sn⁴⁺-oxygen vacancy associates. The type of main defect may reportedly vary depending on the defect engineering strategies used, such as irradiation, heat treatment, chemical reduction, and doping. However, this study devised a new defect formation method called LCP, which differs from existing methods. When the LCP process was applied based on bare SnO₂, a reduction reaction in which the bond between Sn and O was broken occurred in the early stage, and an oxidation reaction in which the bond between Sn and O was formed in the later stage is mainly summarized. This occurred because as seen in a previous report [39], although there are various defect formation methods and types of defects in the same SnO₂ material, oxygen vacancies are the most common (nearly 70 out of 85 cases) [39]. In addition, they play an important role in SnO₂ gas-sensing. Specifically, the atomic ratio of Sn to O on the SnO₂ NR surface can be gauged as a function of LCP duration. It is crucial to note the spectral position of the oxygen peak and its corresponding binding energy values. Generally, the oxygen peak for SnO₂ NRs is located at 529.88 eV [40] (Fig. 5a-b). However, upon LCP treatment between 1S5T and 4S5T, the peak shifts to 530.47 eV at 1S5T (Figs. 5c), 530.82 eV at 2S5T (Figs. 5d), 530.01 eV at 3S5T (Fig. 5e), and 329.98 eV at 4S5T (Fig. 5f), respectively. As shown in Fig. 6, a quantitative analysis of the lattice oxygen (O_L), oxygen vacancy (O_V), and chemisorbed oxygen (O_C) for each oxygen peak was performed in detail [41]. In bare SnO₂ NRs, O_L played a leading role compared to O_V and O_C (Fig. 6a), whereas in 1S5T LCP, O_V played a leading role compared to O_L and O_C (Fig. 6b). From 2S5T to 4S5T LCP, the chemisorbed O appeared to be relatively prominent (Fig. 6c-e). The changing trends of the three oxygen species from the bare to 4S5T LCP are shown in Fig. 6f. Namely, as the LCP process increased, if O_V increased, O_L decreased, and as O_C increased, O_V decreased. Therefore, the type of oxygen contributing to the sample varied depending on the

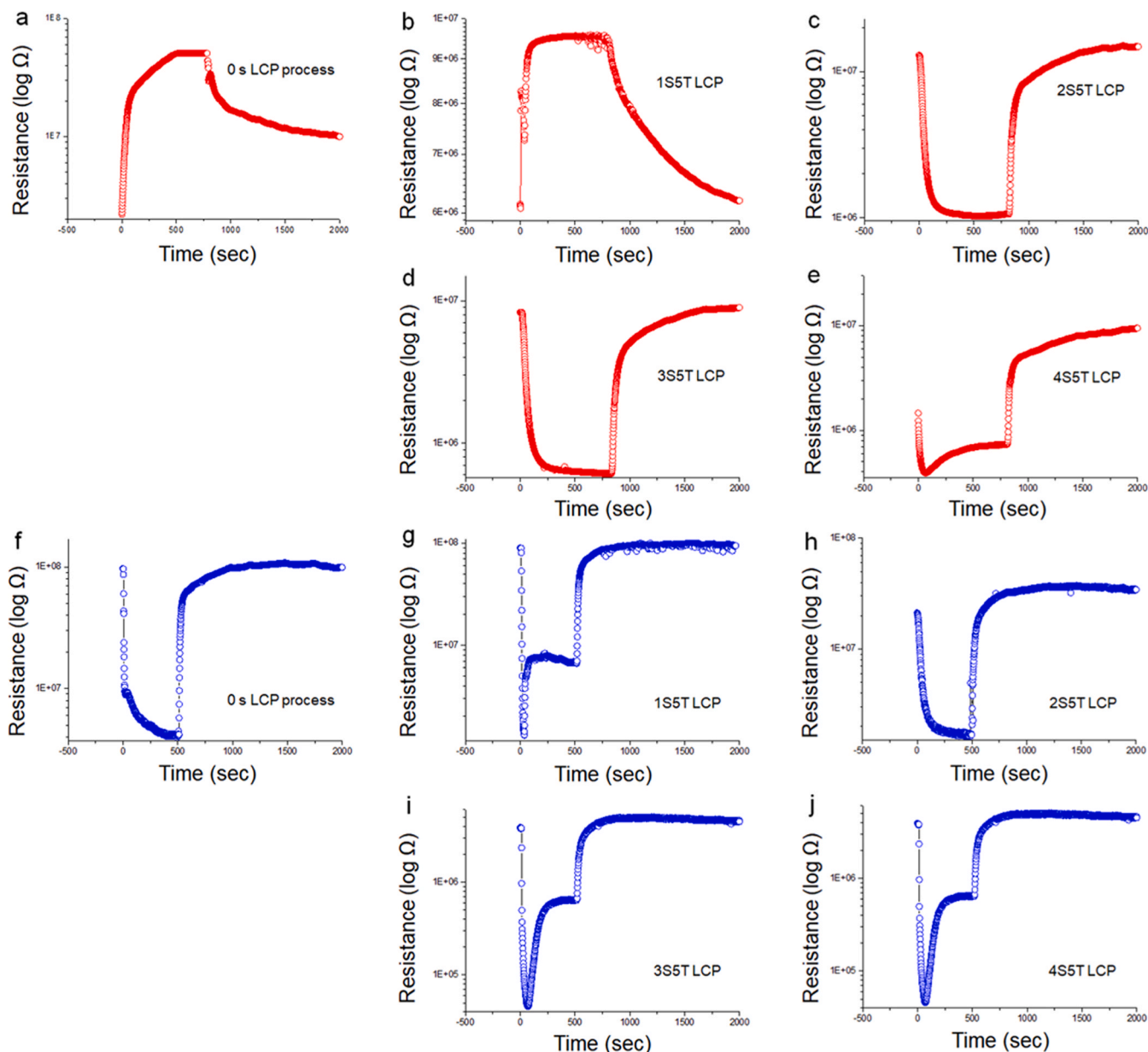


Fig. 9. Gas sensing responses to 50 ppm concentrations of (a-e) NO_2 and (f-j) H_2 at 300 °C in SnO_2 NRs subjected to various LCP conditions ranging from 1S5T to 4S5T.

LCP. Although these peaks correspond to non-equilibrium Sn-O bonds, the spectral shifts indicate reduction and oxidation reactions, respectively, thus corroborating our earlier findings.

UPS was employed to measure the work function and the valence band maximum of SnO_2 NRs subjected to different LCP conditions (Fig. 7). For each LCP treatment, the measured work function-valence band maximum pairs were: 0 s LCP at 4.8 eV-4.0 eV (Fig. 7a-c), 1S5T LCP at 4.4 eV-3.75 eV (Fig. 7d-f), and 4S5T LCP at 4.2 eV-3.6 eV (Fig. 7g-i). These results suggest that the work function and its difference from the valence band maximum serve as indirect indicators of the electrical type transition (from n-type to p-type) triggered by LCP. The results measured by the UPS are shown in terms of the major energy bands in Fig. 8; Fig. 8a presents bare SnO_2 NRs without an LCP process, and has a work function of 4.8 eV and a valence band maximum of 4.0 eV. However, for 1S5T LCP, where oxygen vacancies appear, the work function and valence band maximum values are 4.4 eV and 3.75 eV, respectively; for 4S5T LCP, where chemisorbed O appears, they

are 4.2 eV and 3.6 eV, respectively. Namely, as the LCP process progresses, the difference between the work function and the valence band maximum decreases. As the LCP progressed, the VB_{max} value gradually decreased from the vacuum state and/or E_{F} , indirectly implying the possibility of the n-type bare SnO_2 NRs being changed to p-type semiconductors through the LCP process.

As seen in Table S1, the core inquiry of this study revolves around the extent of alteration in mobile carriers within original SnO_2 NRs upon adsorption of oxygen or other target gases onto the SnO_2 surface. To investigate this, we examined changes in resistance for different gases—specifically, oxidizing gas NO_2 and reducing gas H_2 —at a process temperature of 300 °C, where the sensing characteristics are most optimal. As depicted in Fig. 9, SnO_2 NRs exposed to 50 ppm NO_2 gas displayed an increase in resistance when treated with 0 s LCP and 1S5T (Fig. 9a-b), and a decrease in resistance when subjected to 2S5T-4S5T LCP conditions (Fig. 9c-e). This observation suggests that, at the 0 s LCP and 1S5T states, SnO_2 functions as an n-type semiconductor primarily

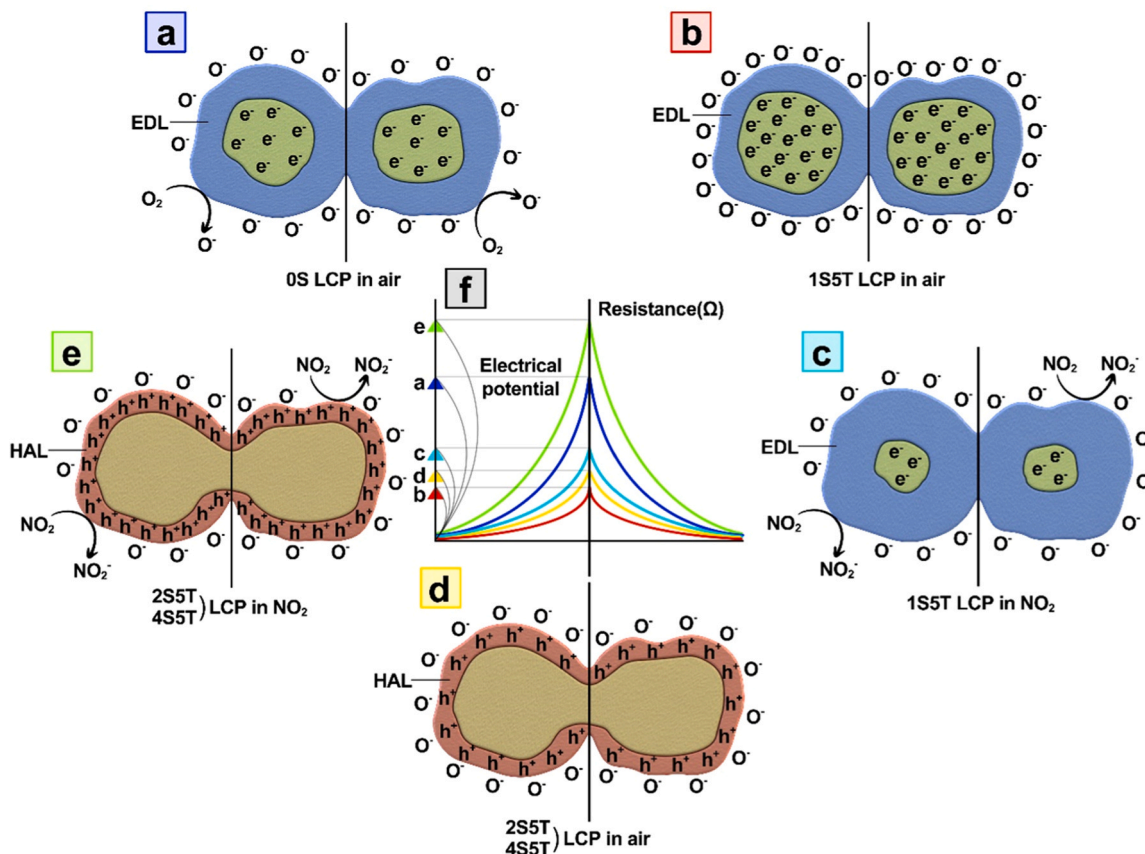


Fig. 10. Gas sensing mechanisms for 50 ppm NO₂ at 300 °C. Panel (a) illustrates the formation of an electron depletion layer (EDL) in SnO₂ NRs at 0 s LCP in an air environment. Panels (b) and (c) show modifications in oxygen species and EDL in SnO_{2-x} NRs under 1S5T LCP in air and NO₂, respectively. Panels (d) and (e) display alterations in oxygen species and hole accumulation layer (HAL) in SnO_{2+x} NRs under 2S⁵T–4S5T LCP in air and NO₂, respectively. Panel (f) indicates the electric potential corresponding to each stage from panels (a) to (e).

carrying electrons. Conversely, at the 2S⁵T–4S5T states, SnO₂ assumes a p-type semiconductor role where the dominant carriers are holes. In contrast, exposure to 50 ppm H₂, a reducing gas, manifested characteristics consistent with n-type semiconductivity across all LCP conditions, including 0 s LCP (Fig. 9f–j). Consequently, while SnO₂ NRs exhibit bidirectional semiconductive behavior in response to NO₂, they demonstrate unidirectional n-type characteristics for H₂, rendering them unsuitable as generalized semiconductor gas sensors.

Initial investigations indicate that atmospheric oxygen is adsorbed at the terminal points of SnO₂ NRs. This occurs because oxygen possesses higher electron affinity compared to SnO₂; it captures electrons from SnO₂ upon surface adsorption, subsequently creating an electron depletion layer (EDL) on the SnO₂ surface [42]. Concurrently, the form of adsorbed oxygen ions varies as a function of temperature. Specifically, the reactions involving adsorbed oxygen species are differentiated by temperature ranges (i.e., O_{2(ads)}} + e⁻ → O_{2(ads)}⁻ (T < 100 °C), O_{2(ads)}⁻ + 2e⁻ → 2 O_{(ads)}⁻ (100 °C < T < 300 °C), O_{(ads)}⁻ + e⁻ → O_{(ads)}²⁻ (T > 300 °C)) [43,44]. Thus, given our process temperature of 300 °C, it can be concluded that a mixture of O_{(ads)}⁻ and O_{(ads)}²⁻ species is present.}}}}}}}

Variations in oxygen concentration on the surface of SnO₂ NRs, induced by LCP, significantly influence the sensing mechanisms for oxidizing and reducing gases. Consider NO₂, an oxidizing gas, which can be categorized into five scenarios depending on LCP conditions, as illustrated in Fig. 10.

Initially, under 0 s LCP conditions, atmospheric oxygen abstracts electrons from the surface of SnO₂ NRs, thereby forming an EDL (Fig. 10a). In contrast, for 1S5T LCP conditions, the energy is focused locally, disrupting existing SnO₂ bonds and generating a plethora of O vacancies in the surface layer. Consequently, as demonstrated in

Fig. 10b, the thickness of the electron channeling layer increases relative to that in the 0 s LCP state, leading to a further reduction in EDL thickness. When NO₂ is introduced, it captures additional electrons from the SnO₂ NR surface (Fig. 10c). As the EDL thickens, the thickness of the electron channeling layer contracts, exhibiting the characteristics of a typical n-type semiconductor, where resistance augments.

Conversely, when LCP conditions are escalated to 2S⁵T–4S5T, the laser's energy is sustained at a single point for an extended duration, promoting chemisorbed O over oxygen vacancies. This results in the formation of a hole accumulation layer (HAL) [45,46] on the SnO₂ NR surface, as illustrated in Fig. 10d. When NO₂ gas is introduced under these circumstances, the HAL thickens, diverging from the 1S5T LCP conditions. Concurrently, the thickness of the hole channeling layer directed towards the SnO₂ NR surface expands, characterizing a typical p-type semiconductor in which resistance diminishes (Fig. 10e). The electrical potential at each stage is delineated in Fig. 10f. To summarize, SnO₂ NRs subjected to 1S5T LCP conditions manifest a relatively high electrical potential, characteristic of n-type semiconductors. In contrast, SnO₂ NRs treated with 2S⁵T–4S5T LCP conditions display a lower electrical potential, indicative of p-type semiconductors.

In the case of H₂, a reducing gas, the behavior deviates from that of NO₂ based on LCP conditions. The first two stages under LCP conditions parallel those observed for NO₂ (Fig. 11a–b). When H₂ is introduced, it donates additional electrons to the surface of SnO₂ NRs, consequently augmenting the thickness of the electron channeling layer within the SnO₂ NRs. This leads to a decrease in resistance, indicative of a typical n-type semiconductor behavior (Fig. 11c). Notably, under more extreme LCP conditions (2S⁵T–4S5T), the introduction of H₂ does not merely mirror the behavior of NO₂. As illustrated in Fig. 11d, severe LCP

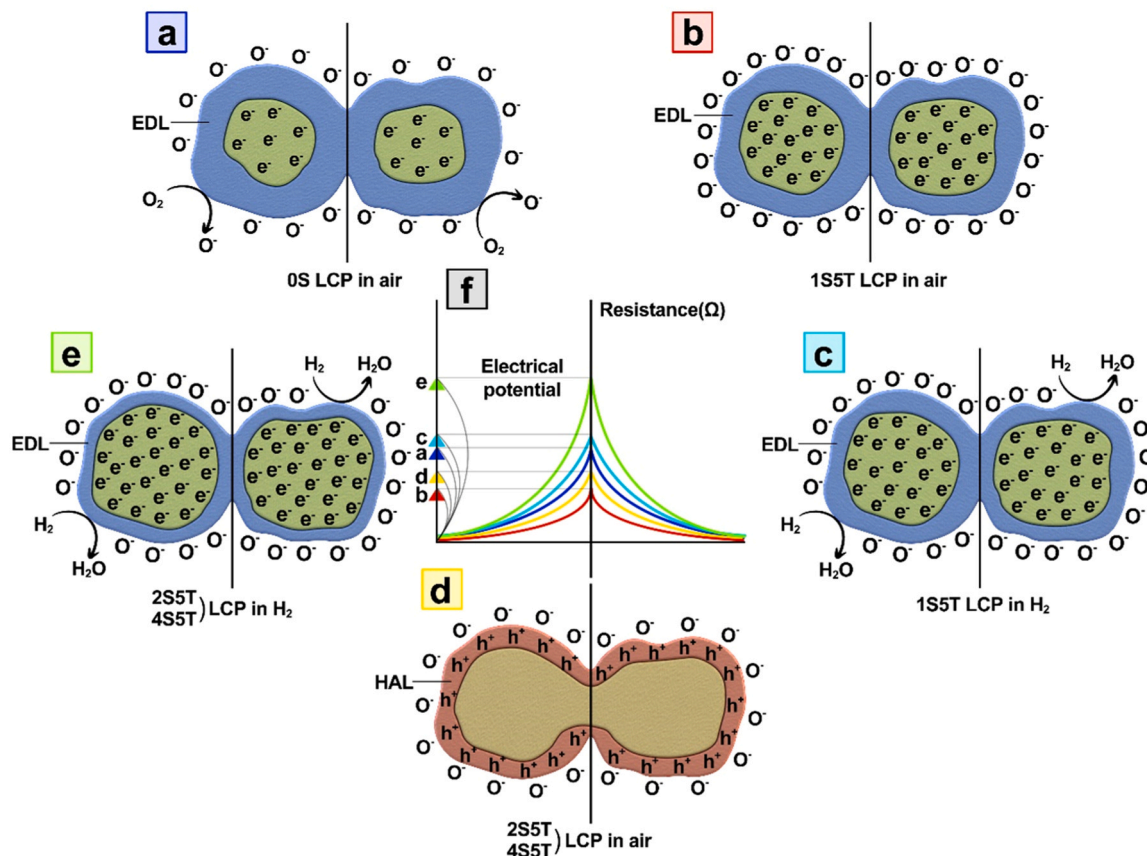


Fig. 11. Gas sensing mechanism for 50 ppm H_2 gas at 300 °C. Panel (a) portrays the formation of an electron depletion layer (EDL) in SnO_2 NRs subjected to 0 s LCP in an air environment. Panel (b) illustrates modifications in O^- and EDL in SnO_{2-x} NRs under 1S5T LCP in air. Panel (c) shows similar changes but under 1S5T LCP in an H_2 environment. Panel (d) elucidates alterations in oxygen species and a hole accumulation layer (HAL) in SnO_{2+x} NRs under 2S⁵T–4S5T LCP in air. Panel (e) details similar alterations under 2S⁵T–4S5T LCP in H_2 . Panel (f) specifies the electric potential at each stage ranging from panels (a) to (e).

conditions cause the aggregation of ambient oxygen, forming chemisorbed O rather than vacancies and establishing a HAL on the SnO_2 NR surface. However, unlike NO_2 , the electrons contributed by H_2 suffice to counterbalance the existing HAL, thus negating any transition to p-type characteristics (Fig. 11e). Consequently, resistance diminishes as the electron channeling layer's thickness increases (Fig. 11f).

In summary, while NO_2 exhibits both n-type and p-type semiconductor behaviors in response to varying oxygen concentrations under different LCP conditions, H_2 consistently maintains n-type characteristics irrespective of these changes. As shown in Fig. 12, this divergence in chemical sensitization under identical electronic states (i. e., the same LCP conditions) may be attributed to disparities in bonding energies between NO_2 and H_2 [47]. This arises from the difference in the chemical reaction of NO_2 (i. e., $\text{NO}_{2(\text{gas})} + \text{e}^- \rightarrow \text{NO}_{2(\text{ads})}^-$, $\text{NO}_{2(\text{ads})}^- + \text{O}_{2(\text{ads})}^- + 2\text{e}^- \rightarrow \text{NO}_{2(\text{ads})}^- + 2\text{O}_{(\text{ads})}^-$, $\text{NO}_{2(\text{ads})}^- + \text{O}_{(\text{ads})}^- + 2\text{e}^- \rightarrow \text{NO}_{(\text{gas})} + 2\text{O}_{(\text{ads})}^-$ [48]) and H_2 (i. e., $\text{H}_{2(\text{gas})} \rightarrow \text{H}_{2(\text{ads})}$, $\text{H}_{2(\text{ads})} + \text{O}_{(\text{ads})}^- \rightarrow \text{H}_2\text{O}_{(\text{gas})} + \text{e}^-$ [49]). As demonstrated by the two aforementioned equations, NO_2 easily dissociates into NO and O in the gas phase, whereas H_2 hardly dissociates. Therefore, NO_2 can serve as a source of atomic oxygen. Namely, as NO_2 dissociation occurred, the amount of chemisorbed O increased between the target gas and surface of the SnO_2 NBs+NRs, which further expanded the HAL on the sample surface. In particular, as the LCP process progressed from bare-1S5 LCP to 2S⁵T–4S5T LCP, the p-type conductivity of the SnO_2 NBs + NRs improved. In contrast, H_2 immediately reduced the electron depletion and restored the n-type surface conductivity of the SnO_2 NBs+NRs. This phenomenon in H_2 occurred across the entire range from the bare SnO_2 NRs to the 4S5T LCP. Namely, more chemisorbed oxygen induces such a high electron depletion, resulting in an inverted conductivity layer (i. e., HAL).

Subsequently, NO_2 increases the hole concentration and improves the p-conductivity, whereas H_2 promptly reduces electron depletion and recovers the n-type surface conductivity in the SnO_2 NRs. Therefore, while NO_2 can transition between the two types of semiconductors, H_2 remains singular.

The foregoing analyses offer a nuanced perspective on the significance and interplay of electronic and chemical sensitization in p-n transitions. Such insights are anticipated to find applicability in diverse domains, thereby extending the utility of these concepts for future investigations and applications.

4. Conclusions

NO_2 and H_2 gas sensing by the SnO_2 NRs was performed using a new LCP process that varied from the existing light-activated gas sensors. When the point energy LCP, which concentrates the laser beam at a singular location, is employed on SnO_2 NRs, disparate chemical reactions ensue depending on the LCP duration. Specifically, 1S5T SnO_2 NRs undergo a reduction reaction involving Sn and O, whereas 2S⁵T–4S5T SnO_2 NRs are subject to an oxidation reaction of the same elements. These varied reactions result in distinct electronic states within the SnO_2 NRs, dictated by the LCP conditions, and consequently, divergent sensing mechanisms are manifested based on the chemical reaction of the target gas. For example, in the presence of NO_2 , the 1S5T LCP process fosters n-type semiconductor behavior predominantly characterized by O vacancies. Conversely, under 2S⁵T–4S5T LCP conditions, p-type behavior prevails, attributed largely to the formation of chemisorbed O. In contrast, for the reducing gas H_2 , a consistent n-type behavior is observed across all LCP conditions. Thus, the ability to tailor

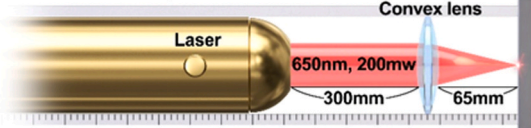
Bond energy (kJ/mol)	Gas	Bond	Structural formula
1076.5	CO	C—O	C≡O
436.8	CH ₃ OH	H—OCH ₃	$\begin{array}{c} \text{H} \\ \\ \text{H}-\text{C}-\text{O}-\text{H} \\ \\ \text{H} \end{array}$
436.0	C ₂ H ₅ OH	H—OC ₂ H ₅	$\begin{array}{c} \text{H} \quad \text{H} \\ \quad \\ \text{H}-\text{C}-\text{C}-\text{O}-\text{H} \\ \quad \\ \text{H} \quad \text{H} \end{array}$
436.0	H ₂	H—H	H—H
431.0	C ₆ H ₆	H—C ₆ H ₅	$\begin{array}{c} \text{H} \\ \\ \text{H}-\text{C}=\text{C}=\text{C}-\text{H} \\ // \quad \backslash \quad / \\ \text{H}-\text{C}=\text{C}=\text{C}-\text{H} \\ \\ \text{H} \end{array}$
413.4	CH ₄	H—CH ₃	$\begin{array}{c} \text{H} \\ \\ \text{H}-\text{C}-\text{H} \\ \\ \text{H} \end{array}$
393.0	CH ₃ COCH ₃	H—CH ₂ COCH ₃	$\begin{array}{c} \text{H} \quad \text{H} \quad \text{H} \\ \quad \quad \\ \text{H}-\text{C}-\text{C}-\text{O}-\text{H} \\ \quad \\ \text{H} \quad \text{H} \end{array}$
391.0	NH ₃	H—NH ₂	$\begin{array}{c} \text{H}-\text{N}-\text{H} \\ \\ \text{H} \end{array}$
381.0	H ₂ S	H—SH	$\begin{array}{c} \text{H} \\ \backslash \quad / \\ \text{S} \\ / \quad \backslash \\ \text{H} \end{array}$
			
305.0	NO ₂	O—NO	$\begin{array}{c} \text{O} \\ \backslash \quad / \\ \text{N} \\ / \quad \backslash \\ \text{O} \end{array}$

Fig. 12. Comparative assessment of bond energies and molecular structures in diverse gaseous environments. This figure demonstrates how LCP process conditions permit the fine-tuning of the energy landscape that governs the bonding behavior between oxidizing and reducing gases.

the specific type and degree of semiconductor properties to align with user requirements, based on LCP conditions, represents a straightforward yet effective surface modification technique. This approach offers the potential for wide-ranging applicability to diverse processes and applications.

CRediT authorship contribution statement

Yang Hyunseong: Visualization, Investigation, Data curation, Conceptualization. **Jin Changhyun:** Writing – original draft, Visualization, Investigation, Data curation, Conceptualization. **Lee Wooyoung:** Writing – review & editing, Supervision, Project administration. **Lee Kyu Hyoung:** Writing – review & editing, Supervision, Project administration.

Declaration of Competing Interest

The authors declare that they have no known competing financial interests or personal relationships that could have appeared to influence the work reported in this paper.

Data availability

Data will be made available on request.

Acknowledgments

This research was supported by the National Research Foundation of Korea (NRF) grant funded by the Korea government (MIST) (No. NRF-2022M3H4A3053304, National Core Materials Research Center (Platform type)). This work was supported by the Technology Innovation

Program ('20013621', Center for Super Critical Material Industrial Technology) funded By the Ministry of Trade, Industry & Energy (MOTIE, Korea). This research was supported by the Basic Science Research Program through the National Research Foundation of Korea (NRF) funded by the Ministry of Education (NRF-2019R1A6A1A11055660 and RS-2023-00243422). Changhyun Jin was supported by the Korea Initiative for fostering University of Research and Innovation (KIURI) Program of the National Research Foundation (NRF) funded by the Korean government (MSIT) (NRF-2020M3H1A1077207).

Appendix A. Supporting information

Supplementary data associated with this article can be found in the online version at [doi:10.1016/j.snb.2024.135482](https://doi.org/10.1016/j.snb.2024.135482).

References

- [1] S.T. Kochuveedu, Y.H. Jang, D.H. Kim, A study on the mechanism for the interaction of light with noble metal-metal oxide semiconductor nanostructures for various photophysical applications, *Chem. Soc. Rev.* 42 (2013) 8467–8493.
- [2] X. Yu, T.J. Marks, A. Facchetti, Metal oxides for optoelectronic applications, *Nat. Mater.* 15 (2016) 383–396.
- [3] J.M. Caruge, J.E. Halpert, V. Bulović, M.G. Bawendi, Colloidal quantum-dot light-emitting diodes with metal-oxide charge transport layers, *Nat. Photonics* 2 (2008) 247–250.
- [4] N. Wu, Q. Zhang, C. Zhu, D.S.H. Chan, M.F. Li, N. Balasubramanian, A. Chin, D. L. Kwong, Alternative surface passivation on germanium for metal-oxide-semiconductor applications with high-k gate dielectric, *Appl. Phys. Lett.* 85 (2004), 4127–2129.
- [5] M.M. Khan, S.F. Adil, A. Al-Mayouf, Metal oxides as photocatalysts, *J. Saudi Chem. Soc.* 19 (2015) 462–463.
- [6] W. Ouyang, F. Teng, J.H. He, X. Fang, Enhancing the photoelectric performance of photodetectors based on metal oxide semiconductors by charge-carrier engineering, *Adv. Funct. Mater.* 29 (2019) 1807672.
- [7] J. Zhang, Z. Qin, D. Zeng, C. Xie, Metal-oxide-semiconductor based gas sensors: screening, preparation, and integration, *Phys. Chem. Chem. Phys.* 19 (2017) 6313–6329.
- [8] Y. Cheng, B. Ren, K. Xu, I. Jeerapan, H. Chen, Z. Li, J.Z. Ou, Recent progress in intrinsic and stimulated room-temperature gas sensors enabled by low-dimensional materials, *J. Mater. Chem.* 9 (2021) 3026–3051.
- [9] Z. Cui, K. Yang, Y. Shen, Z. Yuan, Y. Dong, P. Yuan, E. Li, Toxic gas molecules adsorbed on intrinsic and defective WS₂: gas sensing and detection, *Appl. Surf. Sci.* 613 (2023) 155978.
- [10] C.N. Wang, Y.L. Li, F.L. Gong, Y.H. Zhang, S.M. Fang, H.L. Zhang, Advances in doped ZnO nanostructures for gas sensor, *Chem. Rec.* 20 (2020) 1553–1567.
- [11] X. Kou, F. Meng, K. Chen, T. Wang, P. Sun, F. Liu, X. Yan, Y. Sun, F. Liu, K. Shimannoe, G. Lu, High-performance acetone gas sensor based on Ru-doped SnO₂ nanofibers, *Sens. Actuators B Chem.* 320 (2020) 128292.
- [12] P. Cheng, F. Dang, Y. Wang, J. Gao, L. Xu, C. Wang, L. Lv, X. Li, B. Zhang, B. Liu, Gas sensor towards n-butanol at low temperature detection: hierarchical flower-like Ni-doped Co₃O₄ based on solvent-dependent synthesis, *Sens. Actuators B Chem.* 328 (2021) 129028.
- [13] J.H. Kim, A. Mirzaei, H.W. Kim, S.S. Kim, Low-voltage-driven sensors based on ZnO nanowires for room-temperature detection of NO₂ and CO gases, *ACS Appl. Mater. Interfaces* 11 (2019) 24172–24183.
- [14] J. Liu, W. Xue, G. jin, Z. Zhai, J. Lv, W. Hong, Y. Chen, Preparation of tin oxide quantum dots in aqueous solution and applications in semiconductor gas sensors, *Nanomaterials* 9 (2019) 240.
- [15] L. Sacco, S. Forel, I. Florea, C.S. Cojocaru, Ultra-sensitive NO₂ gas sensors based on single-wall carbon nanotube field effect transistors: Monitoring from ppm to ppb level, *Carbon* 157 (2020) 631–639.
- [16] J. Wang, H. Shen, Y. Xia, S. Komarneni, Light-activated room-temperature gas sensors based on metal oxide nanostructures: a review on recent advances, *Ceram. Int.* 47 (2021) 7353–7368.
- [17] G. Li, Z. Sun, D. Zhang, Q. Xu, L. Meng, Y. Qin, Mechanism of sensitivity enhancement of a ZnO nanofilm gas sensor by UV light illumination, *ACS Sens* 4 (2019) 1577–1585.
- [18] I. Cho, Y.C. Sim, M. Cho, Y.H. Cho, I. Park, Monolithic micro light-emitting diode/metal oxide nanowire gas sensor with microwatt-level power consumption, *ACS Sens.* 5 (2020) 563–570.
- [19] B. Zhang, N. Bao, T. Wang, Y. Xu, Y. Dong, Y. Ni, P. Yu, Q. Wei, J. Wang, L. Guo, Y. Xia, High-performance room temperature NO₂ gas sensor based on visible light irradiated In₂O₃ nanowires, *J. Alloy. Compd.* 867 (2021) 159076.
- [20] S.K.T. Thathsara, C.J. Harrison, R.K. Hocking, M. Shafiei, Photoactive semiconducting metal oxides: hydrogen gas sensing mechanisms, *Int. J. Hydrog. Energy* 47 (2022) 18208–18227.
- [21] Y.J. Kwon, H.W. Kim, W.C. Ko, H. Choi, Y.H. Ko, Y.K. Jeong, Laser-engineered oxygen vacancies for improving the NO₂ sensing performance of SnO₂ nanowires, *J. Mater. Chem. A* 7 (2019) 27205–27211.
- [22] H. Zhang, L. Liu, C. Huang, S. Liang, G. Jiang, Enhanced acetone gas sensing performance of ZnO polyhedrons decorated with LaFeO₃ nanoparticles, *Mater. Res. Express* (2023).
- [23] L.H. Slewa, T.A. Abbas, N.M. Ahmad, Effect of Sn doping and annealing on the morphology, structural, optical, and electrical properties of 3D (micro/nano) V₂O₅ sphere for high sensitivity pH-EGFET sensor, *Sens. Actuators B Chem.* 305 (2020) 127515.
- [24] E.I. Naik, T.S.S.K. Naik, E. Pradeepa, S. Singh, H.S.B. Naik, Design and fabrication of an innovative electrochemical sensor based on Mg-doped ZnO nanoparticles for the detection of toxic catechol, *Mater. Chem. Phys.* 281 (2022) 125860.
- [25] Y. Xu, T. Ma, Y. Zhao, L. Zheng, X. Liu, J. Zhang, Multi-metal functionalized tungsten oxide nanowires enabling ultra-sensitive detection of trimethylamine, *Sens. Actuators B Chem.* 300 (2019) 127042.
- [26] P. Hao, G. Qiu, P. Song, Z. Yang, Q. Wang, Construction of porous LaFeO₃ microspheres decorated with NiO nanosheets for high response ethanol gas sensors, *Appl. Surf. Sci.* 515 (2020) 146025.
- [27] V.S. Bhati, M. Kumar, R. Banerjee, Gas sensing performance of 2D nanomaterials/metal oxide nanocomposites: a review, *J. Mater. Chem. C* 9 (2021) 8776–8808.
- [28] A. Marikutsa, A. Novikova, M. Rummyantseva, N. Khmelevsky, A. Gaskov, Comparison of Au-functionalized semiconductor metal oxides in sensitivity to VOC, *Sens. Actuator B-Chem.* 326 (2021) 128980.
- [29] S. Brahma, Y.W. Yeh, J.L. Huang, C.P. Liu, Cu-doped p-type ZnO nanostructures as unique acetone sensor at room temperature (~ 25C), *Appl. Surf. Sci.* 564 (2021) 150351.
- [30] W. Li, H. Zhang, X. Zhang, G. Qin, H. Li, Y. Xiong, L. Ye, H. Ruan, C. Tong, C. Kong, L. Fang, Non-axial NO-VZn shallow acceptor complexes in nitrogen implanted p-type ZnO thin films, *Appl. Surf. Sci.* 529 (2020) 147168.
- [31] Y. Du, X. Gao, X. Meng, Preparation and characterization of single-phased n-type CuO film by DC magnetron sputtering, *Phys. B* 560 (2019) 37–40.
- [32] M.M. Islam, M.O. Liedke, D. Winarski, M. Butterling, A. Wagner, P. Hosemann, Y. Wang, B. Ueberuaga, F.A. Selim, Chemical manipulation of hydrogen induced high p-type and n-type conductivity in Ga₂O₃, *Sci. Rep.* 10 (2020) 6134.
- [33] J. Kim, H. Park, D. Kim, S. Yang, S. Song, Y. Choi, H. Kim, J.-S. Bae, C.T. Le, Y. S. Kim, M. Yang, K. Ihm, K.-S. Lee, C.-H. Park, S. Park, Bi doping stimulation on the visible-light absorption of In₂O₃ ceramics, *J. Alloy. Compd.* 878 (2021) 160339.
- [34] J. Wang, Z. Liu, B. Kong, X. An, M. Zhang, W. Wang, Intrinsic point defects and the n- and p-type dopability in α - and β -Bi₂O₃ photocatalysts, *Phys. Chem. Chem. Phys.* 25 (2023) 14417–14429.
- [35] S. Baturay, A. Tombak, D. Batibay, Y.S. Ocak, n-Type conductivity of CuO thin films by metal doping, *Appl. Surf. Sci.* 477 (2019) 91–95.
- [36] H. Sun, M.H. Liao, S.C. Chen, Z.Y. Li, P.C. Lin, S.M. Song, Synthesis and characterization of n-type NiO: Al thin films for fabrication of pn NiO homojunctions, *J. Phy. D. -Appl. Phys.* 51 (2018) 105109.
- [37] P. Gupta, T. Dutta, S. Mal, J. Narayan, Controlled p-type to n-type conductivity transformation in NiO thin films by ultraviolet-laser irradiation, *J. Appl. Phys.* 111 (2012).
- [38] M.D. Lee, G.J. Lee, I. Nam, M.A. Abbas, J.H. Bang, Exploring the effect of cation vacancies in TiO₂: lithiation behavior of n-type and p-type TiO₂, *ACS Appl. Mater. Interfaces* 14 (2022) 6560–6569.
- [39] Y. Xiong, Y. Lin, X. Wang, Y. Zhao, J. Tian, Defect engineering on SnO₂ nanomaterials for enhanced gas sensing performances, *Adv. Powder Mater.* 1 (2022) 100033.
- [40] L. Liu, Y. Wang, K. Guan, Y. Liu, Y. Li, F. Sun, X. Wang, C. Zhang, S. Feng, T. Zhang, Influence of oxygen vacancies on the performance of SnO₂ gas sensing by near-ambient pressure XPS studies, *Sens. Actuators B Chem.* 393 (2023) 134252.
- [41] X. Guan, P. Luo, X. Li, Y. Yu, D. Chen, L. Zhang, One-step facile synthesis of hierarchically porous nitrogen-doped SnO₂ nanoparticles with ultrahigh surface area for enhanced lithium storage performance, *Int. J. Electrochem. Sci.* 13 (2018) 5667–5680.
- [42] X.T. Yin, J. Li, Q. Wang, D. Dastan, Z.C. Shi, N. Alharbi, H. Garmestani, X.-M. Tan, Y. Liu, X.-G. Ma, Opposite sensing response of heterojunction gas sensors based on SnO₂-Cr₂O₃ nanocomposites to H₂ against CO and its selectivity mechanism, *Langmuir* 37 (2021) 13548–13558.
- [43] F. Li, S. Ruan, N. Zhang, Y. Yin, S. Guo, Y. Chen, H. Zhang, C. Li, Synthesis and characterization of Cr-doped WO₃ nanofibers for conductometric sensors with high xylene sensitivity, *Sens. Actuators B Chem.* 265 (2018) 355–364.
- [44] A. Mirzaei, K. Janghorban, B. Hashemi, M. Bonyani, S.G. Leonardi, G. Neri, A novel gas sensor based on Ag/Fe₂O₃ core-shell nanocomposites, *Ceram. Int.* 42 (2016) 18974–18982.
- [45] S. Zhou, L. Yao, H. Mei, K.G. Dassios, L. Cheng, L. Zhang, Zero-expanded gas sensing of chiral-rotating chemiresistive SiCuOC structures, *Chem. Mat.* 34 (2022) 7167–7180.
- [46] S. Wang, J. Cao, W. Cui, L. Fan, X. Li, D. Li, T. Zhang, One-dimensional porous Co₃O₄ rectangular rods for enhanced acetone gas sensing properties, *Sens. Actuators B Chem.* 297 (2019) 126746.
- [47] J. Shi, Z. Cheng, L. Gao, Y. Zhang, J. Xu, H. Zhao, Facile synthesis of reduced graphene oxide/hexagonal WO₃ nanosheets composites with enhanced H₂S sensing properties, *Sens. Actuators B Chem.* 230 (2016) 736–745.
- [48] Y. Nagarjuna, Y.-J. Hsiao, TeO₂ doped ZnO nanostructure for the enhanced NO₂ gas sensing on MEMS sensor device, *Sens. Actuator B-Chem.* 401 (2024) 134891.
- [49] S. Lu, Y. Zhang, J. Liu, H.-Y. Li, Z. Hu, X. Luo, N. Gao, B. Zhang, J. Jiang, A. Zhong, J. Luo, H. Liu, Sensitive H₂ gas sensors based on SnO₂ nanowires, *Sens. Actuator B-Chem.* 345 (2021) 130334.

Changhyun Jin received his Ph.D. degree in Materials Science and Engineering from Inha University, South Korea, in 2013. He is currently a research professor at the Department of

Materials Science and Engineering, Yonsei University. His areas of interest are (i) synthesis of inorganic nanostructures with controlled dimension, (ii) interaction between inorganic nanostructures and chemicals, and (iii) optical properties of nanostructure arrays and aggregates.

Hyunseong Yang received a Bachelor's degree in Bio medical Engineering at Yonsei University in 2022. Since 2022, he is currently studying on semiconductor gas sensors as a Master's student under the guidance of Prof. Wooyoung Lee at Yonsei University.

Kyu Hyong Lee is currently a professor in the Department of Materials Science and Engineering at Yonsei University in Seoul, Korea. He received his Ph.D. in ceramic engineering from Yonsei University in 2005. From 2005–2007, he worked as a postdoctoral research fellow at Nagoya University. Since 2007, he has been a research staff member and since 2010 project leader at the Samsung Advanced Institute of Technology. His research activity has focused on the development of high-performance thermoelectric materials and functional oxides.

Wooyoung Lee is the Underwood distinguished professor of the Department of Materials Science and Engineering at Yonsei University in Korea. He is also the Director of the Center for Super Critical Material Industrial Technology, National Core Materials Research Center and the institute of Korea Initiative for Fostering University of Research and Innovation. He is the President of The Korean Magnetics Society and a regular member of the National Academy of Engineering of Korea. In recent years, his research interests have centered on hydrogen sensors, various metal oxide semiconducting gas sensors, and breath analyzers. He is also studying rare-earth permanent magnets and thermoelectric materials and devices. He has received a number of awards in nano-related research areas including a Prime Minister Award (2023) in Nano Korea 2023, SeAH-Haiam Fellowship Award (2018) in The Korean Institute of Metals and Materials and a Service Merit Medal (2008) from the Government of Korea due to his contribution to the development of intellectual properties. He has authored and co-authored over 280 publications and has edited three special books on nanostructured materials and devices